

# Design and fabrication of 3D-printed gradient scaffolds for osteochondral tissue engineering

Ana Rita Mendes 99641, Maria Simões 99693, Mariana Costa 99703 and Rebeca Friedrich 99708

**Abstract**—Osteochondral injuries pose a major problem due to their high incidence and lack of effective treatment. This tissue is an interface between bone and cartilage, whose different characteristics hinder the regeneration of both. Tissue engineering strategies have emerged as an alternative to overcome this issue, in which scaffolds play a crucial role by providing structural support for tissue growth. Our principal aim - developing an automated way of designing these structures - was successfully achieved. In addition, several scaffolds were designed and printed, including one with gradients along the height. Moreover, morphological and mechanical characterization was performed by SEM and compression tests. These allowed, respectively, confirmation of scaffolds' correct printing and verification that larger pore sizes result in structures with lower stability. In the future, it is important to invest in the automation of more scaffold designs and study their effects on cell culture.

## I. INTRODUCTION

CARTILAGE and osteochondral unit-related injuries are becoming increasingly prevalent in today's society. [1] Among these, osteoarthritis (OA) is one of the most frequent chronic health pathologies, commonly leading to disability. It is a degenerative joint condition that occurs when the cartilage that cushions the extremities of the bone deteriorates and is consequently associated with great pain, instability, stiffness, and swelling. [2]

Several techniques have been used to treat these conditions, such as articular chondrocyte implantation, employed for large lesions; microfracture, indicated for small lesions; autograft; and mosaicplasty. However, all these methods exhibit limitations, including not only a lack of integration but also inadequate cartilage formation. In fact, fibrocartilaginous tissue is formed instead of hyaline cartilage, which is mechanically inferior. [3]

These limitations relate to the complexity of the osteochondral unit. This tissue consists of 90% of hyaline cartilage, 5% of a calcified cartilage layer, and 5% of subchondral bone and it is placed at the extremity of long bones, containing several gradients that accompany the evolution from the bone to cartilage. [4] The superficial cartilage zone is formed by small and flattened chondrocytes which become increasingly rounded in morphology as the depth increases. As compared with cartilage, the subchondral bone is stiffer and less pliable, being responsible not only for absorbing shocks but also for providing structural support and supplying nutrients. [5]

These two tissues have completely dissimilar structural, electrical, biochemical, biomechanical, and metabolic properties, namely, it is known that native cartilage lacks vascularization and has a low cell density of chondrocytes unlike the bone, which is vascular and porous. The properties of articular cartilage explain its limited capacity for self-renewal. [2]

Thus, the only form to cure osteochondral injuries is by resorting to techniques that allow the reconstruction of both the cartilage and the underlying bone, being essential that these consider the differences in cell number, orientation, and extracellular matrix fiber arrangement along the osteochondral tissue as well as the gradient of mineralization and pore sizes. [2] [4]

Therefore, tissue engineering techniques such as combining progenitor cells, scaffolds, and growth-stimulating signals emerged. [6] A scaffold is any material designed with the purpose of adapting to the affected area of an injury and is typically formed by polymeric materials that provide structural support and stimulate tissue development. These structures are a promising solution as they allow imitation of the structural and functional profile of the original tissue. After *in vitro* expansion, cells seeded on scaffolds are intended to be implanted in the patient. [7]

Hence, the main goal of this project is to design scaffolds that manage to recreate the stress distribution, biomechanical factors' action, and the cartilage-bone interface's porous architecture gradient. Depending on the tissue considered, pore size gradients are essential due to differences in vascular network formation, cell migration, adhesion, and nutrient flow. [2] Scaffolds with a small pore size (about 100  $\mu\text{m}$ ) create hypoxic conditions that favor chondrogenesis, whereas a larger pore size ( $> 300 \mu\text{m}$ ) induces osteogenesis and is essential for vascularization and bone growth. [8]

Over time, new scaffold design techniques were developed. These include fiber-bonding, solvent casting, membrane lamination, thermally induced phase separation, gas foaming, or freeze-drying processes. [9] However, the results obtained were considered unsatisfactory, since these techniques failed to obtain scaffolds with a well-defined porous structure, adequate mechanical properties, and control the reproducibility of scaffold morphology. [2]

The limitations of conventional techniques gave rise to rapid prototyping (RP) technology. The most used to build scaffolds are three-dimensional printing (3DP), which requires organic solvents, multi-phase jet solidification, and shape deposition manufacturing. [9]

In this project, our group used additive manufacturing (AM), a type of extrusion printing, which allows the manufacture of complex scaffolds through a computer-aided design (CAD) model. More specifically, fused deposition modelling (FDM) was used, which compared to other methods does not require any solvent and allows ease in material processing. In this extrusion-based process, thin thermoplastic filaments are melted and extruded through a computer-controlled movable nozzle tip and deposited onto a platform layer by layer

according to a pattern chosen by the user, in order to generate a 3D construct. [6] [9] [10] This technique offers an efficient and fast method to obtain scaffolds with the desired size, shape, and structure, adapted to the lesion area of each patient.

For that purpose, both natural and synthetic materials have been used in the construction of 3D polymeric scaffolds. Natural polymers are generally proteins or polysaccharides such as fibrin, collagen, and chitosan and are highly biocompatible and biodegradable. [6] However, since its degradation kinetics is uncontrolled, and it lacks sufficient mechanical properties, synthetic scaffolds are usually resorted to since they contain high purity and adjustable mechanical and chemical properties. [9]

The most common materials that allow the construction of 3D scaffolds in biomedicine are poly( $\epsilon$ -caprolactone) (PCL), poly(D, L-lactic-co-glycolic acid) (PLGA), and polylactic acid (PLA) mainly due to their biodegradability, biocompatibility, and good processability. [11] PCL is an ideal material for the FDM fabrication process as a consequence of its flexibility, structural stability, and high resistance to environmental conditions such as temperature and moisture. Nevertheless, due to the hydrophobic nature of PCL, unplanned cellular attachment has been reported. [6] PLGA is also a popular biodegradable polymer, having advantages such as adjustability, and satisfactory toughness. [12]

PLA is a polyester largely used for the manufacture of bone scaffolds that has been approved by FDA (Food and Drug Administration) for direct contact with biological fluids and has advantages such as low cost and adjustability since its properties can be aligned to a specific application by modification of the initial composition. The major concern of PLA is that its degradation can lead to an abrupt release of the acidic degradation by-products, consequently generating an inflammatory response, which restrains tissue regeneration. Other drawbacks include poor toughness and low hydrophilicity. [11]

In the present study, porous PLA-based scaffolds with high interconnectivity were designed through a programming interface present in the CAD software Fusion 360, in order to turn its design as automatic, versatile, and reproducible as possible. This is extremely important as it makes it feasible to vary parameters such as layer height and fiber dimension without starting the design from scratch. Subsequently, the scaffolds were fabricated via 3D printing containing porosity gradients and variations in fibers' angular orientations to mimic the disparity in the composition of the native osteochondral tissue. The printed constructs were then subjected to mechanical tests, such as uniaxial mechanical compression, for the purpose of ensuring that the biomaterials were developed with adequate mechanical resistance. Lastly, they were also evaluated for consistency and pore size using scanning electron microscopy (SEM).

Categorically, the main aims of this study are focused on: (1) Automation of scaffolds design; (2) Demonstration of the benefits of incorporating porosity gradients and different fiber orientations within polymeric scaffolds to mimic the osteochondral anatomy; (3) Investigation of scaffolds morphology and mechanical properties.

In the future, it is extremely relevant to combine these techniques with various external physical factors such as mechanical, electrical, and magnetic stimulation, that can magnify specific cellular and tissue behaviours. [13]

#### *A. Automation of the problem*

Using 3D-printed scaffolds for replacing osteochondral tissue is still an experimental technology, and the research conducted on this subject is in the very early stages. According to the U.S. National Library of Medicine database of clinical trials, there are no clinical trials on any progress level that involve 3D printed scaffolds for tissue repairing, which evidentiates that further investigation and testing are necessary before it can be considered a valid treatment option. [14]

In this regard, a countless number of scaffolds with different configurations and properties will need to be designed and produced to conduct the necessary structural, mechanical, and biocompatibility tests, among many others. Since 3D modelling is a task that requires high attention to detail and precision, designing a scaffold from scratch can divert many hours of work that could be spent on more important research tasks.

To address this challenge and attempt to expedite the production of scaffolds, we developed Python scripts that can be run on Fusion 360 to instantly generate 3D scaffolds with different configurations. The Fusion 360 API allows the user to employ scripts to either automate certain design processes or generate entire objects from scratch. We used libraries developed by the Fusion team - which are available for consultation online - to automate through code the repetitive operations required to build a scaffold. [15] These scripts will be briefly described further along.

#### *B. Code implementation*

We developed a total of seven scripts that allow the user to explore different configurations, as shown in Table I. However, throughout this paper, we will only focus on three of these.

The user that desires to generate a specific scaffold only has to choose the script with the desired specifications and insert some parameters such as the diameter of the fibers and the scaffold's length, height, width, gradient of porosity and displacement of the fibers. Immediately after running the script, the scaffold will appear on the interface and is ready to be exported and printed.

This approach not only saves time and effort but also ensures consistency and accuracy in the design process, assuring that the geometrical constraints are correctly defined. This is especially important when quick and repeated changes to design parameters are required to iterate through different configurations.

To provide a general view of the potential of these automatic scripts, we produced and printed one of each scaffold. A summary of the main advantages and considerations of each of those scaffolds will also be explored further along on this report.

Although the user is not required to understand the code specifications to generate the scaffold, it can be beneficial to have a basic understanding of the underlying principles:

TABLE I: List of scripts produced and their characteristics.

Name	Shape Of Fiber Section	Scaffold Body Geometry	Relative Position Of Fibers	Spacing Gradient Between Fibers
Circular1	Circular	Parallelepiped	Perpendicular	No
Quadrangular1	Quadrangular	Parallelepiped	Perpendicular	No
Cilindrico1 *	Circular	Cylindrical	Perpendicular	No
Sec_quad_cilindrico1	Quadrangular	Cylindrical	Perpendicular	No
Angulos_cilindrico *	Circular	Cylindrical	Desired Angle	No
Angulos_camadas	Circular	Parallelepiped	Desired Angle	No
Porosidade *	Circular	Parallelepiped	Perpendicular	Yes

\* Scripts explored throughout this project.

- 1) The section of a fiber is sketched (circle or square) taking into account the diameter inserted by the user;
- 2) It is then extruded to the length given as input;
- 3) Steps 1 and 2 are repeated on a perpendicular plane, to generate two perpendicular single fibers;
- 4) It is created a rectangular pattern that replicates both single fibers horizontally and vertically, generating alternated parallel layers of perpendicular fibers, with the desired spacing between each fiber;
- 5) In case the scaffold follows a cylindrical geometry, a cylindrical box is cut from the structure.

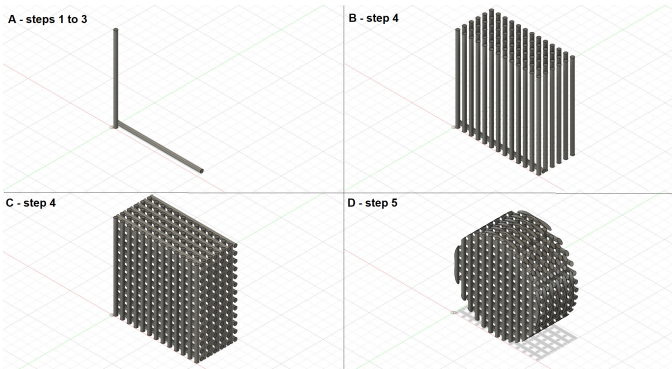


Fig. 1: Summary of the automated steps: A - Generating two parallel fibers; B - Using a rectangular pattern to generate the first set of layers; C - Using a rectangular pattern to generate the second set of layers; D - Cutting a cylindrical box if needed.

For the scripts that generate scaffolds with non-perpendicular fibers between each layer, the principles are the same but the single fibers initially generated are obliquus instead of perpendicular.

Before implementing the code solution, rigorous calculus were made to assure the validity of the automatic scaffolds produced, guaranteeing that all the geometrical and mechanical constraints were correct.

All the scripts developed are thoroughly commented to facilitate their understanding and allow their adaptation to the production of more complex scaffolds. They are ready to be used for the generation of scaffolds on an academic context but can also be used as a starting point for the development of more refined tools and libraries, since 3D modelling through code is not a very intuitive task. The implementation was based on the most common necessities presented to us when introduced to this project, but it can be modified and expanded

upon to meet specific requirements since little to no resources are available for automatic scaffold design.

In this way, our aim was not only to develop a tool that allows the user to instantly generate scaffolds, but also to encourage and contribute to further exploration in the field of scaffold design and fabrication.

## II. MATERIALS AND METHODS

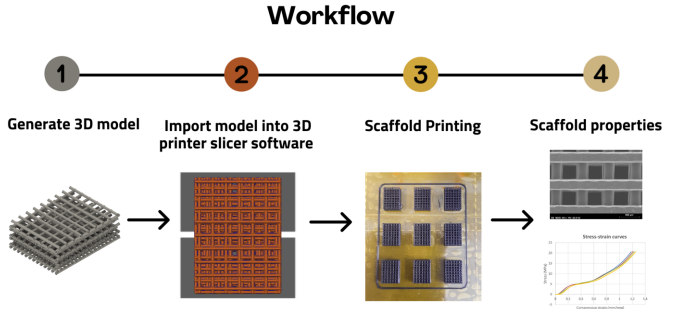


Fig. 2: Workflow performed (x7): 1 - Generation of a 3D model; 2 - Importation of the model into a printer slicer software; 3 - Scaffold printing; 4 - Scaffold properties averiguacion.

### A. Scaffolds structure

In this project, seven scaffolds were designed using both the graphical and the programming interface of the CAD software Fusion 360. Four were designed to contain variation in the fiber's angular orientation, two were intended to imitate a cylindrical shape, and another aimed for porosity gradient incorporation.

It is known that different scaffold geometries originate dissimilar pore shapes, which, consequently, serve divergent biological responses. In addition, porosity and filament orientation are the most important aspects affecting mechanical properties. [10]

Fiber orientations of 0°/90° and 0°/60°/120° cause filaments to cross over at the same positions for each layer. It is acknowledged that a larger contact area between layers forms a stronger solid polymer column. Thus, the elastic modulus is higher in this case, which means greater resistance to elastic deformation under stress. On the contrary, the filaments of scaffolds with a lay-down pattern of 0°/45°/90° only cross over

TABLE II: Scaffolds' parameters.

Scaffold	Lay-down pattern (°)	Shape	Length (mm)	Breadth (mm)	Height (mm)	Pore size (mm)	Fiber diameter (mm)	Gradient* (%)
1	0/30/60	Cuboid	10	10	4.8	0.4	0.4	-
2	0/45/90	Cuboid	10	10	4.8	0.4	0.4	-
3	0/60/120	Cuboid	10	10	4.8	0.4	0.4	-
4	0/90	Cuboid	10	10	4.8	0.4	0.4	-
5	0/90	Cuboid	10	7.5	3.6	0.3-0.845	0.3	23
6	0/90	Cylindrical	10	10	4.8	0.4	0.4	-
7	0/30/150	Cylindrical	10	10	4.8	0.4	0.4	-

\* Porosity increase rate relative to the previous layer.

at different points on different layers, which results in a weaker structure. [10]

On the other hand, cylindrical scaffolds allow to avoid sharp edges and corners and to better imitate the composition and structure of the osteon concentric arrangement. [16]

Furthermore, the pore size of the scaffolds affects cell seeding and proliferation. While a pore size of 350  $\mu\text{m}$  is ideal for proliferation, cell seeding occurs more efficiently with a pore size of 800  $\mu\text{m}$ . [10] Associated with the necessity of mimicking the osteochondral tissue, it becomes extremely relevant the design of a scaffold with a porosity gradient.

For each scaffold sketched, it was possible to vary the orientation angle of the fibers, the size and gradient of the pores, the fibers section, and the dimensions and shape of the scaffolds, which therefore leads to alterations in porosity and interconnectivity. The parameters chosen for each scaffold are presented in Table II.

In all designed scaffolds, a circular section of fiber was used as well as repeated layers. Additionally, it was alternated the use of aligned and staggered filaments, in which the top filaments, whose horizontal position was offset  $x$  mm, where  $x$  equals the value of the fiber diameter, were alternately staggered in relation to filaments in lower layers. Staggered filaments were used in scaffolds 4 and 5 as they have a lower elastic modulus than aligned filaments, meaning that they are not as resistant to compression and are prone to collapsing in a concertina manner as the stress is concentrated at specific points. Papers have reported that cell seeding is most efficient on scaffolds containing these characteristics. In aligned filaments, the fibers intersect in the same positions, creating a solid column, and, therefore, are more able to resist compression. [10]

### B. 3D printing method

Fused deposition modelling (FDM) was the technique used to print the CAD-designed scaffolds presented in the previous section. It is necessary to generate the G-code which contains the commands for the printer movements that enable the CAD model structure to be printed. For that, a .step file containing the scaffold's design was created in Autodesk Fusion 360 and then imported to PrusaSlicer, the software used for the generation of G-code. This code was subsequently transferred to the printer (Original Prusa i3 MK3S & MK3S +MMU2S Single 0.25 mm nozzle) via an SD card.

FDM utilizes thermoresponsive polymers that are heated above their glass transition temperature and then deposited

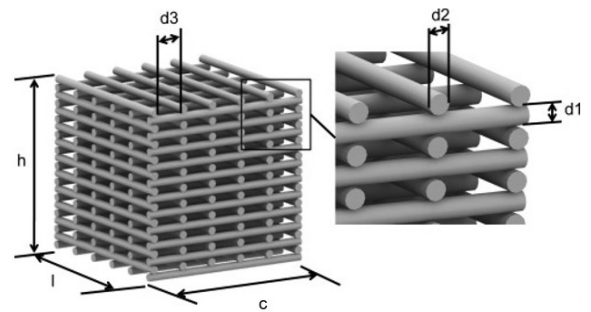


Fig. 3: Scaffold's structure parameters:  $h$  - height;  $l$  - breadth;  $c$  - length;  $d1$  - layer thickness;  $d2$  - fiber diameter;  $d3$  - pore size. (Sobral, J. et al., 2011, *Acta Biomaterialia*, 7(3).)

into a solid platform. In this experiment, the 3D printing material chosen was conductive PLA, which is specifically designed to transmit electric current and therefore increase scaffold bioactivity. [17] PLA has a low glass temperature, around 60°C, which makes it a popular material choice for FDM printing. The ideal nozzle temperature is around 210 °C [18] which is in accordance with the nozzle temperature value predefined for PLA in the software used. Once the fiber's diameter was mostly 0.4 mm, a layer height of 0.2 mm was set (except for scaffold 5), making it necessary two layers to produce one proper layer of fibers. For each scaffold design, 9 instances were printed in order to compensate possible damage when removing the scaffolds from the printing bed.

The main printing process parameters are summarised in the following table:

TABLE III: Printing process parameters.

Material	Conductive PLA
Nozzle temperature	210 °C
Bed temperature	60 °C
Nozzle diameter	0.25 mm
Layer height	0.2 mm
Printing speed	45 mm/s

### C. Scaffold characterization

1) Optical microscopy: In order to visualize the shape of the pores and confirm the correct design and printing of the scaffolds, optical microscopy (model LEICA DMI3000B, Leica Microsystems, Germany), equipped with a digital camera (Nikon DXM1200F, Nikon Instruments Inc., Japan), was performed, with an image magnification of 40x. The

scale bar was set to 100  $\mu\text{m}$ .

2) *Scanning electron microscopy*: Scanning electron microscopy (SEM) (model S2400, Hitachi, Tokyo, Japan) was executed in order to morphologically characterize the scaffolds as it allows the visualization of different pore sizes.

Primarily, all specimens were sputter-coated with a thin conductive layer of gold/palladium (model Q150T ES, Quorum Technologies, Laughton, East Sussex, UK). Then, the images were taken with an accelerating voltage of 20 kV and a magnification of 50x. The scale bar was set to 500  $\mu\text{m}$ .

An image processing program, ImageJ, was used to confirm the distance between fibers, the fibers' angular orientation and to assess the printing fidelity, which compares the printed scaffold with the designed scaffold.

3) *Mechanical testing*: Due to time limitations, it wasn't possible to realize mechanical tests with our impressed scaffolds. To illustrate the procedure to study mechanical properties of scaffolds, results previously obtained with PCL scaffolds, by IBB (*Institute for Bioengineering and Biosciences, Instituto Superior Técnico*) were used, since PCL is also a greatly used synthetic polymer in tissue engineering.

Using an Instron machine (model 5544, Instron, Norwood, MA, USA) outfitted with a 2 kN load cell and a 50 mm diameter cylindrical compression plate, PCL scaffolds (lay-down pattern: 0°/90°; cuboid shape; dimensions: 10 mm  $\times$  10 mm  $\times$  3 mm; porosities: 100  $\mu\text{m}$ , 300  $\mu\text{m}$ , and 600  $\mu\text{m}$ ) were mechanically assessed under compressive testing in order to distinguish the mechanical properties of scaffolds with distinct porosities. According to ASTM guidelines, an extension rate of 1 mm/min was employed, with n = 4 samples for each condition. The Bluehill 3 program (Instron) was used to examine the results that were collected.

With these results, a plot of stress dispersion (MPa) vs strain (mm/mm) was generated for each of the 12 scaffolds, and the slope of their initial linear region (which corresponds to the compressive modulus of elasticity, E) was calculated. The average of the E obtained for each sample of a particular type of scaffold was then computed. By measuring the standard deviation, the level of E value dispersion for each kind of scaffold was determined. Microsoft Excel was used to complete each of these computations.

4) *Statistical Analysis*: Microsoft Excel was used to perform statistical analysis. All results were expressed as mean values with standard deviations. One-way analysis of variance (ANOVA) was used and differences were considered significant for  $p$ -value < 0.05.

### III. RESULTS AND DISCUSSION

#### A. *Scaffolds' design*

The scaffolds designed using both the graphical (1, 2, 3, and 4) and the Python-programming interface (5, 6, and 7) of the CAD software Fusion 360 are exhibited in Figure 4 and Figure 5. In all of them, it is possible to visualize the top view, which reveals the fibers' angular orientation and the

honeycomb-like shape of the pores, ranging from a rhombus (1 and 7), hexagonal (2), triangular (2 and 3), and quadrangular (4, 5 and 6) morphology.

For the scaffolds containing staggered filaments (4 and 5) and a porosity gradient (5), it became relevant to analyze the side view. This view allows the observation of the porosity gradient along the height (5), with the pore size increasing by 23% compared to the previous layer. Consequently, a decrease in the number of fibers in each layer is verified.

All designs were automatized, allowing adaptability to changing parameters.

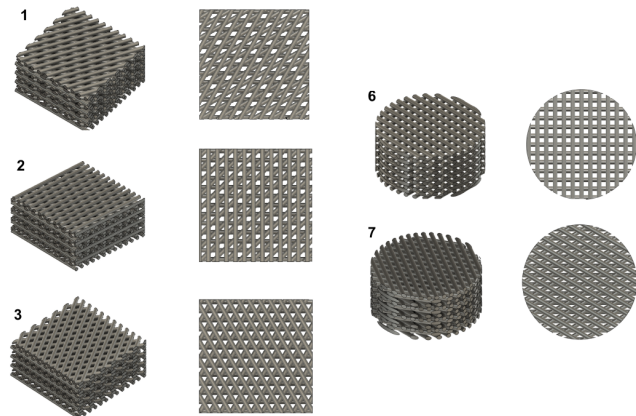


Fig. 4: Designed scaffolds displayed in a 3D and top view. The scaffolds' numeration is in accordance with Table II.

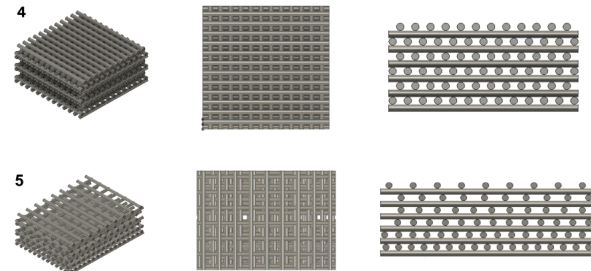


Fig. 5: Designed scaffolds displayed in a 3D, top and side view. The scaffolds' numeration is in accordance with Table II.

#### B. *Scaffolds' printing*

Both the printed scaffolds as well as their optical microscopy images are shown in Figure 6. The images obtained confirmed the shape of the pores according to the angular orientation of the fibers.

Lay-down patterns of 0°/30°/60° (1) and 0°/30°/150° (7) create diamond-shaped pores. For the 0°/60°/120° (3) and 0°/90° (4, 5, and 6) lay-down patterns, forming a triangular and quadrangular pore shape respectively, it is possible to infer the cross-over of the filaments in the same positions, revealing a strong network of interconnected channels, which makes the scaffold more robust and resistant to deformation. The opposite occurs with the 0°/45°/90° (2) lay-down pattern,

which not only establishes a more irregular pore shape (ranging from triangular to hexagonal) but also crosses over at different points, making the polymer structure weaker. [10]

Hence, it is possible to conclude that by varying the angular orientation of the fibers and by forming a sequence on a multilayer scaffold, 3D scaffolds with different pore sizes and shapes can be achieved. It is known that the use of a finer nozzle tip would permit the fabrication of finer scaffolds with more reliable pore sizes and would increase the surface area-to-volume ratio. However, they have disadvantages such as the possibility of clogging and longer printing time. Thus, it is recommended to use a larger nozzle with high carriage speed. [9] [19]

It is also possible to verify the staggered filaments with low material stiffness in image 4, as well as the porosity gradient along the height in image 5 of Figure 6. Pore size could be enlarged and raster angles in consecutive layers could be repeated in order to increase porosity. However, it is necessary to take into account the slacking that could occur due to the lack of strength of the extruded filaments to bridge the wider gap. The values used were considered adequate for tissue engineering of the osteochondral unit. [20]

Additionally, it was confirmed that conductive PLA was the indicated material for scaffold printing, satisfying the smoothness and precision requirements of the printing process. The FDM method was also successful in reproducing the original designs with high fidelity, as it allowed precise control of pore size variation, as has been demonstrated in the past.

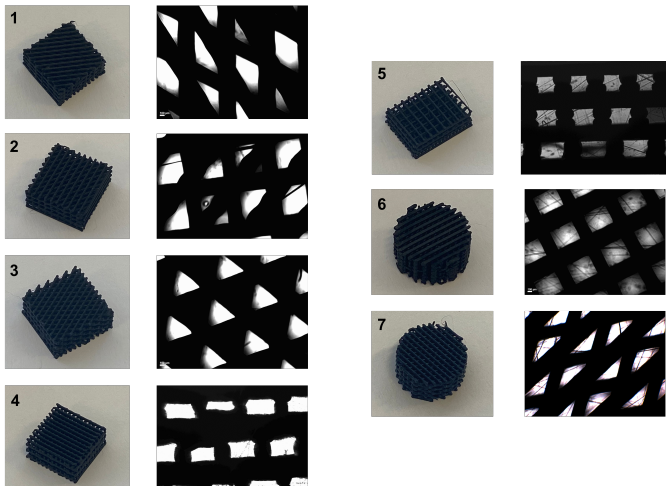


Fig. 6: Printed scaffolds and corresponding images under optical microscope (magnification: 40x; scale bar: 100  $\mu\text{m}$ ). The scaffolds' numeration is in accordance with Table II.

### C. Scaffolds' SEM

The scaffolds' images obtained by scanning electron microscopy (SEM) are exhibited in Figure 8. A scaffold of each condition was evaluated separately using ImageJ, an image processing program, in order to visualize the fibers' angular orientation and to measure the pore size.

Through the high-quality images, it is possible to clearly visualize the honeycomb-like pore patterns as well as to

infer the high interconnectivity between the fibers. Moreover, as the intended pore shape was obtained according to each fibers' angular orientation - lay-down patterns of 0°/30°/60° and 0°/30°/150°, 0°/45°/90°, 0°/60°/120°, and 0°/90° resulted in structures with rhombus, complex polygonal, triangular and quadrangular pores, respectively - it can be inferred that the CAD design was correctly computed and the printing process was properly executed. Image 2 of Figure 8 is the one containing the most errors, both in terms of the pore shape and in relation to the fiber printing, with unwanted waves being noticeable. This may have occurred due to the fragility of the structure or the accumulation of air pockets on the surface during the printing process. A good solution to overcome this problem would be increasing the composite's mechanical properties through the introduction of various coatings. [21]

Images 4 and 6 of Figure 8 distinctly show the difference between aligned and staggered filaments. In image 4 it is possible to differentiate the staggered filaments when observing the lower layers of the scaffold while in image 5 the porosity gradient is visible. In fact, in this image, the filaments show some cracks, possibly due to printing tension.

In order to verify whether there was printing fidelity, that is, whether or not the printed scaffolds turned out to be exact copies of those drawn in the CAD software, measurements of the distance between fibers and statistical analysis were carried out.

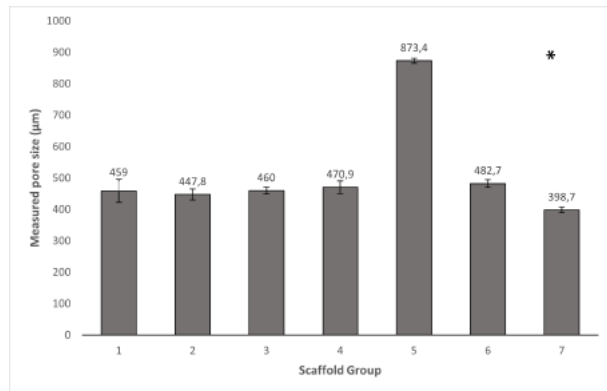


Fig. 7: Measured pore sizes for different PLA-scaffolds' conditions. Values above bars represent the mean, while SD is represented by an error bar ( $n = 4$  per group of scaffolds). The scaffolds' numeration is in accordance with Table II.

The results show that the measured distances between filaments, calculated with ImageJ, are relatively similar to what was expected and defined in the printing process. For all scaffolds the expected pore size was 400  $\mu\text{m}$ , excluding scaffold number 5, whose pore size of the layer with the largest height was intended to be 845  $\mu\text{m}$ . This revealed that the FDM printing worked by allowing the reproducibility of scaffolds micro-architecture.

Relative standard deviation (RSD) values ranged from 0.9 to 7.9%. The standard deviation manifests some dispersion of the measurements, however, these values are considered normal due to the non-rigorous measurement method employed, since parsing with ImageJ is considerably prone to human error. [22]

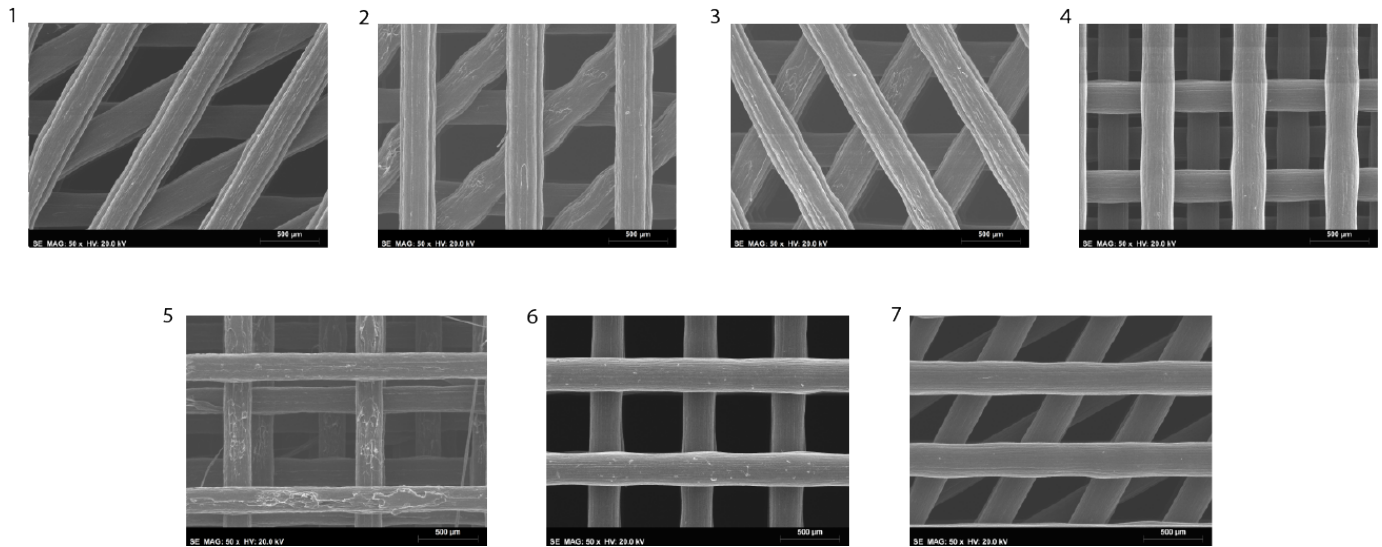


Fig. 8: Scaffolds' SEM images (accelerating voltage: 20 kV; magnification: 50x; scale bar: 500  $\mu\text{m}$ ). The scaffolds' numeration is in accordance with Table II.

No correlation was found between the angular orientation of the fibers and the measured pore size, however, it is noticeable that the smallest difference between the measured and expected result occurred for scaffold number 7 (cylindrical, lay-down pattern: 0°/30°/150°). For lay-down patterns of 0°/90° (4, 5, and 6), it was verified that the discrepancy became more pronounced the smaller the pore size.

TABLE IV: Pore size statistical analysis for different PLA scaffolds. Values represent mean  $\pm$  RSD and relative difference ( $n = 4$  per group of scaffolds).

Scaffold	Mean $\pm$ RDS ( $\mu\text{m} \pm \%$ )	Relative Difference (%)
1	459.0 $\pm$ 7.9	14.75
2	447.8 $\pm$ 3.8	11.95
3	460.0 $\pm$ 2.3	15.0
4	470.9 $\pm$ 4.2	17.725
5	873.4 $\pm$ 0.9	3.4
6	482.7 $\pm$ 2.5	20.7
7	398.7 $\pm$ 2.1	0.3

Percentages of relative difference, which express the pore size excess (in all scaffolds but number 7) in relation to the reference value of each scaffold, were obtained, ranging from 3.4 to 20.7%. This may be acceptable taking into account the possibility of the creation of a more porous structure since the increase in porosity would allow a higher cell seeding capacity due to a larger availability of pore space. [9]

The divergence of results between the different scaffolds was analyzed by using ANOVA. This analysis led to the conclusion that there is a significant difference (\*) among groups ( $p$ -value  $< 0.05$ ). This can be explained by the use of ImageJ, a software associated with human error since the measures are done manually.

Despite these differences, it is possible to assure that both the design and the printing of scaffolds under different conditions were successfully accomplished, allowing the passage to the next step, which is scaffolds' mechanical properties testing.

#### D. Scaffolds' mechanical properties

The stress-strain curves for PCL-scaffolds with different pore sizes (100  $\mu\text{m}$ , 300  $\mu\text{m}$ , and 600  $\mu\text{m}$ ) are disposed in Figure 9, Figure 10 and Figure 11. For each porosity, four samples were analyzed.

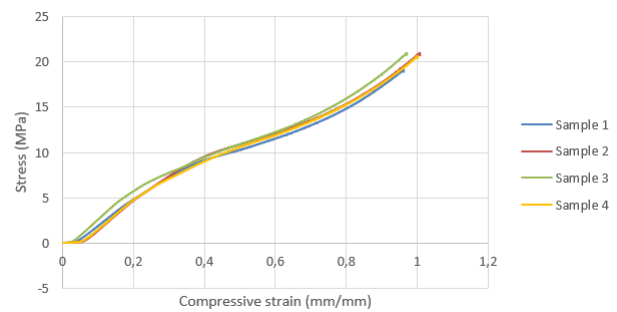


Fig. 9: Stress-strain curves for PCL 100  $\mu\text{m}$  samples (lay-down pattern: 0°/90°; cuboid shape; dimensions: 10 mm  $\times$  10 mm  $\times$  3 mm;  $n = 4$  samples).

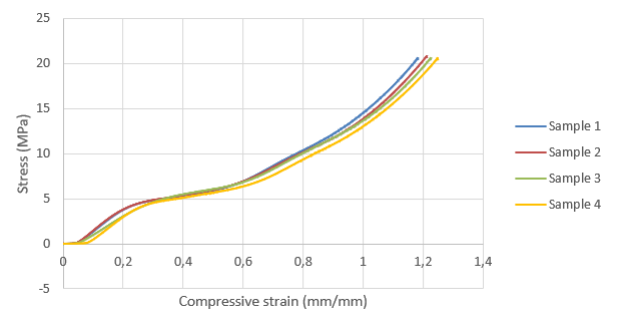


Fig. 10: Stress-strain curves for PCL 300  $\mu\text{m}$  samples (lay-down pattern: 0°/90°; cuboid shape; dimensions: 10 mm  $\times$  10 mm  $\times$  3 mm;  $n = 4$  samples).

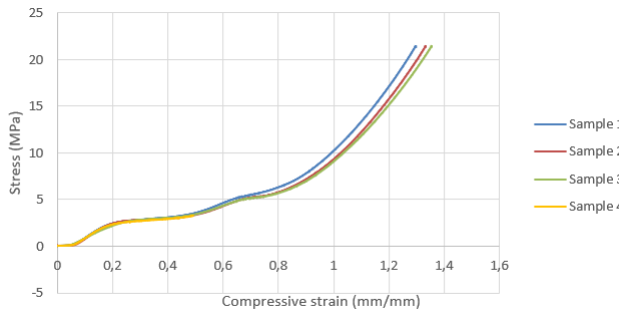


Fig. 11: Stress-strain curves for PCL 600  $\mu\text{m}$  samples (lay-down pattern: 0°/90°; cuboid shape; dimensions: 10 mm  $\times$  10 mm  $\times$  3 mm; n = 4 samples).

TABLE V: Compressive modulus ( $E$ ) and porosity of PCL scaffolds with different pore sizes. Values represent mean  $\pm$  SD (n = 4 per group of porosity).

Porosity ( $\mu\text{m}$ )	Compressive Modulus, $E$ (MPa)
100	$32.7 \pm 1.8$
300	$24.1 \pm 2.3$
600	$18.3 \pm 2.0$

Table V shows that the compressive modulus,  $E$ , decreases as porosity increases, which is expected due to lower stability of the scaffold structure for larger pores. Hence, there is a prominent similarity between scaffolds with greater porosity and the deformable behaviour of the osteochondral unit, when compared with those with lower porosities. [2] The standard deviation is small in the 3 types of scaffolds, which indicates a low degree of  $E$  values' dispersion.

Besides, it is observed that the curves present their three distinct regimes: starting with a linear-elastic regime, followed by a plateau of approximately constant stress, and leading into a final regime of precipitous rising stress. As expected, the stress gradually rises with increasing strain. Also, the curves of the lower porosity scaffolds showed a steeper initial linear-elastic regime and a higher plateau height compared with the ones with larger pores. On the contrary, the larger pore sizes show greater strain values than all the other conditions.

In these tests, the maximum axial force that the samples were able to withstand was around 2000 N. This indicates that the scaffolds produced have good compressive strength and can withstand certain external pressures. For example, bearing in mind that, during walking, the peak axial compression force on the femur is estimated at around 2.5 to 3 times the body weight (which would correspond, in an adult weighing 70 kg, to a maximum axial compression between 1750 and 2100 N), it was concluded that these scaffolds could potentially withstand a walk. However, during running, forces can increase to 4-5 times body weight; and in jumping and other high-impact activities, even greater forces can be generated on the femur, which would therefore not be bearable by these scaffolds. [23]

Furthermore, native human articular cartilage has an elastic compressive modulus ranging from 240 to 1000 kPa, trabecular bone tissue has an elastic compressive modulus ranging from 10 to 20 GPa, and cortical bone has an elastic

compressive modulus ranging from 6.5 to 18.2 MPa. [24] [25] Consequently, these values indicate that our scaffolds wouldn't have a proper support for trabecular bone, but a considerably good one for cortical bone.

To conclude this analysis, Young's modulus are within the expected values for the material used (reported in the range of 4 to 77 MPa for FDM<sup>1</sup> printing). [9]

TABLE VI: Compression strength at yield ( $\sigma_y$ ) and compression yield strain ( $\varepsilon_y$ ) for different porosities of PCL scaffolds. Values represent mean  $\pm$  SD (n = 4 per group of porosity).

Porosity ( $\mu\text{m}$ )	$\sigma_y$ (MPa)	$\varepsilon_y$ (mm/mm)
100	$5.7 \pm 0.6$	$0.2 \pm 0.04$
300	$3.8 \pm 0.2$	$0.2 \pm 0.03$
600	$2.1 \pm 0.1$	$0.2 \pm 0.01$

The intersection of the stress-strain curve and the Young's modulus slope at a strain offset of 0.20% was defined as the compression strength at yield ( $\sigma_y$ ). The compression yield strain ( $\varepsilon_y$ ) was defined as the strain at which the yield occurred when the toe-region was ignored during initial alignment. [9] The results obtained, represented in Table VI, reveal that the measured yield strength is lower when the porosity is higher. Since the minimum required value of yield strength to replace a human trabecular bone is 5 MPa, the scaffold with lower porosity (100  $\mu\text{m}$ ), would be the only type of scaffold that could be applied in this particular region of the bone. [9]

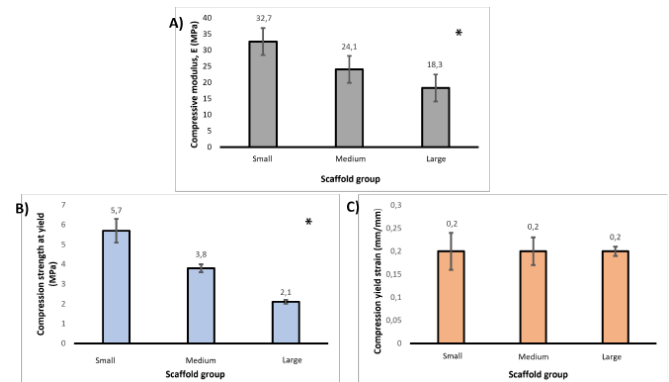


Fig. 12: A) Compressive modulus ( $E$ ) (MPa), B) Compression strength at yield ( $\sigma_y$ ) (MPa), and C) Compression yield strain ( $\varepsilon_y$ ) (mm/mm), for different porosities of PCL scaffolds (small: 100  $\mu\text{m}$ ; medium: 300  $\mu\text{m}$ ; large: 600  $\mu\text{m}$ ). Values above bars represent the mean, while SD is represented by error bars (n = 4 per group of porosity).

These results demonstrate an inverse relationship between porosity and compressive modulus ( $E$ ), and between porosity and compression strength at yield ( $\sigma_y$ ), whereas compression yield strain ( $\varepsilon_y$ ) doesn't seem to have any correlation with differences in porosity.

In fact, by ANOVA statistical test, it is concluded that the differences between  $E$  from different groups of porosity and the  $\sigma_y$  from different porosities are significant (\*), while there is no difference between the means of  $\varepsilon_y$  for the three groups.

<sup>1</sup>Fused Deposition Modeling

By observation of Figure 12, it is evident that in graph A) and B) the values are more divergent between groups, which explains the ANOVA results. Thus, it is possible to conclude that  $E$  and  $\sigma_y$  depends on porosity and not on randomness.

Additionally, it would be interesting not only to investigate the recovery of the stress state, but also to verify the differences in mechanical properties when compression is applied perpendicularly or tangentially in relation to the plane.

#### IV. CONCLUSION

During our project, we managed to achieve the main aim established: the automation of scaffolds' design. The scripts developed enable instantaneous variation of parameters and a wide range of designs. Automation is therefore very useful for researchers, significantly reducing the time spent designing these structures.

Additionally, we aimed to design and print several scaffolds with different shapes (cuboid, cylindrical), fiber orientations (0°/30°/60°, 0°/45°/90°, 0°/60°/120°, and 0°/30°/150°), and incorporate porosity gradients along the height, to achieve the best mechanical properties and also to mimic the natural gradients present in the osteochondral tissue.

The scaffold characterization performed included scanning electron microscopy and mechanical testing. The first method allowed scaffolds' morphological characterization: it was possible to observe in great detail the different pore shapes and also some irregularities resulting from the printing process. Nevertheless, it was confirmed the scaffolds' correct printing, once they were similar to the CAD designs. The mechanical test conducted allowed experimental verification that porosity influences the stiffness of the structures since scaffolds with smaller pore sizes were found to have higher Young's modulus values. This reinforces the idea that the parameters chosen are relevant to the mechanical behaviour of the scaffolds.

As future work, it would be interesting to study the effect of the scaffolds designed in cell culture, namely in the processes of seeding, differentiation, and cell growth. Only after confirming the beneficial effect that scaffolds have in tissue regeneration, will it be possible to proceed to trials using *in vivo* models and, in the future, to perform clinical trials. The ultimate goal of projects involving scaffolds is to develop a valid, effective, and safe treatment strategy to regenerate damaged tissue, in this case, osteochondral tissue.

With the increasing relevance of tissue engineering strategies, it is of great importance the acceleration of the scaffolds manufacture, in order to facilitate the work of researchers. Thus, the automation of scaffolds design represents a huge step forward in this type of strategies.

#### ACKNOWLEDGMENTS

We acknowledge support by IBB (*Institute for Bioengineering and Biosciences, Instituto Superior Técnico*) during the development of this work. The results obtained could not be possible without the help of our advisorship team: João Fernandes da Silva, PhD, and Pedro Marcelino, MSc, and therefore we are deeply grateful for all the assistance provided.

#### REFERENCES

- [1] Allen, K. D.; Thoma, L. M.; Golightly, Y. M. Epidemiology of osteoarthritis. *Osteoarthritis and Cartilage* **2021**, *30*(2), 184–195. <https://doi.org/10.1016/j.joca.2021.04.020>
- [2] Bittner, S. R.; Smith, B. T.; Diaz-Gomez, L.; Hudgins, C. D.; Melchiorri, A. J.; Scott, D.; Fisher, J.; Mikos, A. G. Fabrication and mechanical characterization of 3D printed vertical uniform and gradient scaffolds for bone and osteochondral tissue engineering. *Acta Biomaterialia* **2019**, *90*, 37–48. <https://doi.org/10.1016/j.actbio.2019.03.041>
- [3] Benneker, L.; Cucchiari, M.; Madry, H.; Guilak, F.; Saris, D. B. F.; Stoddart, M.; Wong, M.; Roughley, P. A vision on the future of articular cartilage repair. *European cells & materials* **2014**, *27*, 12-6. <https://doi.org/10.22203/eCM.v027sa03>
- [4] Ansari, S.; Khorshidi, S.; Karkhaneh, A. Engineering of gradient osteochondral tissue: From nature to lab. *Acta Biomaterialia* **2019**, *87*, 41–54. <https://doi.org/10.1016/j.actbio.2019.01.071>
- [5] Wei, W.; Dai, H. Articular cartilage and osteochondral tissue engineering techniques: Recent advances and challenges. *Bioactive Materials* **2021**, *6*(12), 4830–4855. <https://doi.org/10.1016/j.bioactmat.2021.05.011>
- [6] Moura, C. P.; Da Silva, J. S.; Faria, S.; Fernandes, P.; Da Silva, C. L.; Cabral, J. M. S.; Linhardt, R. J.; Da Silva Bartolo, P. J.; Ferreira, F. C. Chondrogenic differentiation of mesenchymal stem/stromal cells on 3D porous poly (ε-caprolactone) scaffolds: Effects of material alkaline treatment and chondroitin sulfate supplementation. *Journal of Bioscience and Bioengineering* **2020**, *129*(6), 756–764. <https://doi.org/10.1016/j.jbiosc.2020.01.004>
- [7] Sobral, J.; Caridade, S. G.; Sousa, R. J.; Mano, J. F.; Reis, R. L. Three-dimensional plotted scaffolds with controlled pore size gradients: Effect of scaffold geometry on mechanical performance and cell seeding efficiency. *Acta Biomaterialia* **2011**, *7*(3), 1009–1018. <https://doi.org/10.1016/j.actbio.2010.11.003>
- [8] Karageorgiou, V.; Kaplan, D. L. Porosity of 3D biomaterial scaffolds and osteogenesis. *Biomaterials* **2005**, *26*(27), 5474–5491. <https://doi.org/10.1016/j.biomaterials.2005.02.002>
- [9] Zein, I.; Hutmacher, D. W.; Tan, K. H.; Teoh, S. H. Fused deposition modeling of novel scaffold architectures for tissue engineering applications. *Biomaterials* **2002**, *23*(4), 1169–1185. [https://doi.org/10.1016/s0142-9612\(01\)00232-0](https://doi.org/10.1016/s0142-9612(01)00232-0)
- [10] Gleadall, A.; Visscher, D. O.; Yang, J.; Thomas, D.; Segal, J. Review of additive manufactured tissue engineering scaffolds: relationship between geometry and performance. *Burns & Trauma Volume* **2018**, *6*. <https://doi.org/10.1186/s41038-018-0121-42-0>
- [11] Donate, R.; Monzón, M.; Alemán-Domínguez, M. E. Additive manufacturing of PLA-based scaffolds intended for bone regeneration and strategies to improve their biological properties. *E-polymers* **2020**, *20*(1), 571–599. <https://doi.org/10.1515/epoly-2020-0046>
- [12] Pan, Z.; Ding, J. Poly(lactide-co-glycolide) porous scaffolds for tissue engineering and regenerative medicine. *Interface Focus* **2012**, *2*(3), 366–377. <https://doi.org/10.1098/rsfs.2011.0123>
- [13] Niu, X.; Li, N.; Du, Z.; Li, X. Integrated gradient tissue-engineered osteochondral scaffolds: Challenges, current efforts and future perspectives. *Bioactive Materials* **2023**, *20*, 574–597. <https://doi.org/10.1016/j.bioactmat.2022.06.011>
- [14] Doyle, S.E.; Snow, F.; Duchi, S.; et al. 3D Printed Multiphasic Scaffolds for Osteochondral Repair: Challenges and Opportunities. *Int. J. Mol. Sci.* **2021**, *22*, 12420. <https://doi.org/10.3390/ijms222212420>.
- [15] Fusion 360 API documentation: Autodesk Fusion 360 Help. Retrieved from <https://help.autodesk.com/view/fusion360/ENU/?guid=GUID-A92A4B10-3781-4925-94C6-47DA85A4F65A> (Last accessed: [30/06/2023]).

- [16] Di Filippo, M.; Amadori, S.; Casolari, S.; Bigi, A.; Dolci, L. S.; Panzavolta, S. Cylindrical Layered Bone Scaffolds with Anisotropic Mechanical Properties as Potential Drug Delivery Systems. *Molecules* **2019**, *24*(10), 1931. <https://doi.org/10.3390/molecules24101931>
- [17] Dixon, D. T.; Gomillion, C. T. Conductive Scaffolds for Bone Tissue Engineering: Current State and Future Outlook. *Journal of Functional Biomaterials* **2021**, *13*(1), 1. <https://doi.org/10.3390/jfb13010001>
- [18] PLA bed temperature & print temperature settings. Retrieved from <https://www.wevolver.com/article/pla-bed-temperature-print-temperature-settings> (Last accessed: [17/06/2023]).
- [19] Ortega, E.; Martinez-De-Pison, F. J.; Pernia-Espinoza, A.; Sanz-Garcia, A. Efficient Fabrication of Polycaprolactone Scaffolds for Printing Hybrid Tissue-Engineered Constructs. *Materials* **2019**, *12*(4), 613. <https://doi.org/10.3390/ma12040613>
- [20] Kim, S. J.; Utsunomiya, H.; Koski, J. A.; Wu, B. M.; Cima, M. J.; Sohn, J. J.; Mukai, K.; Griffith, L. G.; Vacanti, J. P. Survival and Function of Hepatocytes on a Novel Three-Dimensional Synthetic Biodegradable Polymer Scaffold With an Intrinsic Network of Channels. *Annals of Surgery* **1998**, *228*(1), 8–13. <https://doi.org/10.1097/00000658-199807000-00002>
- [21] Baechle-Clayton, M.; Loos, E.; Taheri, M.; Taheri, H. Failures and Flaws in Fused Deposition Modeling (FDM) Additively Manufactured Polymers and Composites. *Journal of Composites Science* **2022**, *6*(7), 202. <https://doi.org/10.3390/jcs6070202>
- [22] Hojat, N.; Gentile, P.; Ferreira, A.; Šiller, L. Automatic pore size measurements from scanning electron microscopy images of porous scaffolds. *Journal of Porous Materials* **2022**, *30*(1), 93–101. <https://doi.org/10.1007/s10934-022-01309-y>
- [23] Van Den Bogert, A. J.; Read, L.; Nigg, B. M. An analysis of hip joint loading during walking, running, and skiing. *Medicine & Science in Sports & Exercise* **1999**, *31*(1), 131–142. <https://doi.org/10.1097/00005768-199901000-00021>
- [24] Beck, E. C.; Barragan, M.; Tadros, M. H.; Gehrke, S. H.; Detamore, M. S. Approaching the compressive modulus of articular cartilage with a decellularized cartilage-based hydrogel. *Acta Biomaterialia* **2016**, *38*, 94–105. <https://doi.org/10.1016/j.actbio.2016.04.019>
- [25] Morgan, E. F.; Unnikrisnan, G. U.; Hussein, A. I. Bone Mechanical Properties in Healthy and Diseased States. *Annual Review of Biomedical Engineering* **2018**, *20*(1), 119–143. <https://doi.org/10.1146/annurev-bioeng-062117-121139>